Shear attenuation and anelastic mechanisms in the central Pacific upper mantle

Zhitu Ma [a,b,*], Colleen A. Dalton [b], Joshua B. Russell [c], James B. Gaherty [c], Greg Hirth [b], Donald W. Forsyth [b]

[a] *State Key Laboratory of Marine Geology, Tongji University, Shanghai, China*
[b] *Department of Earth, Environmental and Planetary Sciences, Brown University, Providence, RI, USA*
[c] *Lamont-Doherty Earth Observatory, Columbia University, Palisades, NY, USA*

ARTICLE INFO

ABSTRACT

We determine the mantle attenuation ($1/Q_\mu$) structure beneath 70 Myr seafloors in the central Pacific. We use long-period (33-100 sec) Rayleigh waves recorded by the NoMelt array of broadband ocean-bottom seismometers. After the removal of tilt and compliance noise, we are able to measure Rayleigh wave phase and amplitude for 125 earthquakes. The compliance correction for ocean wave pressure on the seafloor is particularly important for improving signal-to-noise at periods longer than 55 sec. Attenuation and azimuthally anisotropic phase velocity in the study area are determined by approximating the wavefield as the interference of two plane waves. We find that the amplitude decay of Rayleigh waves across the NoMelt array can be adequately explained using a two-layer model: $Q_\mu = 1400$ in the shallow layer, $Q_\mu = 110$ in the deeper layer, and a transition depth at 70 km, although the sharpness of the transition is not well resolved by the Rayleigh wave data. Notably, Q_μ observed in the NoMelt lithosphere is significantly higher than values in this area from global attenuation models. When compared with lithospheric Q_μ measured at higher frequency ($\sim$3 Hz), the frequency dependence of attenuation is very slight, revising previous interpretations. The effect of anelasticity on shear velocity (V_S) is estimated from the ratio of observed velocity to the predicted anharmonic value. We use laboratory-based parameters to predict attenuation and velocity-dispersion spectra that result from the superposition of a weakly frequency dependent high-temperature background and an absorption peak. We test a large range of frequencies for the position of the absorption peak (f_e) and determine, at each depth, which values of f_e predict Q_μ and V_S that can fit the NoMelt Q_μ and V_S values simultaneously. We show that between depths of 60 and 80 km the seismic models require an increase in f_e by at least 3-4 orders of magnitude. Under the assumption that the absorption peak is caused by elastically accommodated grain-boundary sliding, this increase in f_e reflects a decrease in grain-boundary viscosity of 3-4 orders of magnitude. A likely explanation is an increase in the water content of the mantle, with the base of the dehydrated lid located at $\sim$70-km depth.

© 2020 Elsevier B.V. All rights reserved.

1. Introduction

Seismic attenuation in the mantle occurs as a consequence of transient grain-scale dissipative processes driven by the stress changes imparted by the passage of the seismic waves. Constraining the transient behavior in different regions of the Earth's interior is important for at least two reasons. First, it can be used to place bounds on the physical state of Earth materials, such as tem-

perature and the presence of water and partial melt, because the nature of the transient response is controlled by these and other factors (Abers et al., 2014; Dalton et al., 2017; Ruan et al., 2018; Wei and Wiens, 2018). Second, it can be used to illuminate the grain-scale deformation mechanisms that are responsible for the transient behavior, which may in turn illuminate the mechanisms responsible for steady-state viscous creep (e.g., Freed et al., 2012).

Laboratory experiments provide critical information about the mechanisms causing transient creep and attenuation and the effects of factors including temperature, composition, water, melt, and grain size. They also show how anelasticity causes a frequency-dependent reduction of the shear modulus in addition to the dissi-

* Corresponding author at: State Key Laboratory of Marine Geology, Tongji University, Shanghai, China.
E-mail address: zhitu_ma@tongji.edu.cn (Z. Ma).

pation of energy. Experiments done on olivine, olivine-orthopyroxene, and borneol samples have revealed that the spectrum of attenuation in the frequency domain is comprised of two main components: a pervasive high-temperature background (HTB), wherein attenuation exhibits a weak power-law dependence on frequency and an Arrhenius dependence on temperature, and a plateau or broad peak that becomes prominent at higher frequencies (e.g., Jackson and Faul, 2010; Sundberg and Cooper, 2010; Yamauchi and Takei, 2016; Sasaki et al., 2019).

As a natural laboratory, normal oceanic upper mantle is well suited for studying relationships between attenuation and the mechanisms of anelasticity, in large part because the setting is uncomplicated and the chemical and thermal properties are reasonably well known. Adiabatic decompression of upwelling mantle beneath a mid-ocean ridge leads to partial melting and thereby the creation of oceanic crust and a shallow residual lid that is depleted and dehydrated relative to the unmelted material beneath it (e.g., Hirth and Kohlstedt, 1996; Lee et al., 2005). Samples of abyssal peridotites and mid-ocean ridge basalts interpreted together with petrological experiments define a narrow range of possible peridotite compositions for the lithosphere and asthenosphere (Workman and Hart, 2005; Warren, 2016). Conductive cooling creates a seafloor age-dependent thermal boundary layer, and observations such as bathymetry, heat flow, seismic velocity, and basalt chemistry constrain the thickness of the boundary layer as well as the potential temperature of the mantle adiabat with which it merges (e.g., Parsons and Sclater, 1977; Stein and Stein, 1992; Dalton et al., 2014; Ma and Dalton, 2019).

In this study, we present new high-resolution observations of upper-mantle shear attenuation and velocity beneath 70-Ma seafloor and examine the constraints they provide on the transient rheology as a function of depth. We utilize measurements of Rayleigh wave amplitude and travel time recorded on the NoMelt array of ocean bottom seismometers (OBS) in the central Pacific. The result is a tightly constrained profile of shear attenuation in the depth range 30–200 km that, by representing a 600-km by 400-km area, allows a high level of lateral resolution that is typically not possible in attenuation studies. Furthermore, given our knowledge of the thermal and chemical structure in this setting, it is possible to separate the effects of anelasticity on shear velocity from the effects of elasticity, thereby creating a second datum with sensitivity to the dissipative processes causing attenuation.

A crucial piece of our analysis is removing tilt and compliance noise from the OBS data in order to improve the signal-to-noise ratio and therefore expand the data set at long periods. This process is described in Section 2 and Supplementary Materials Section 1, and the two-plane-wave approach (Forsyth and Li, 2005) used to determine phase velocity and attenuation is described in Section 3. The 1-D attenuation and velocity models are presented in Section 4 interpreted together with laboratory data in Section 5.

2. Data and noise removal

The NoMelt experiment consisted of a broadband OBS deployment (Lin et al., 2016; Russell et al., 2019), a long-period magnetotelluric survey (Sarafian et al., 2015), and an active-source seismic refraction/reflection survey using a short-period OBS array (Mark et al., 2019). In this study we utilize waveforms recorded by the broadband OBS stations, which were deployed from late December 2011 to late December 2012. For all earthquakes in the GCMT catalog (Ekström et al., 2012) with $M_W > 5.5$ that occurred in 2012, we obtain three-component seismic waveform and pressure gauge data from the Data Management Center at the Incorporated Research Institutions for Seismology.

We then follow closely the procedure described in Bell et al. (2014) to remove compliance and tilt noise on the vertical com-

ponent of the OBS data. Details of this procedure can be found in Supplementary Materials Section 1. Examples of waveforms showing the effect of tilt and compliance noise removal are shown in Fig. 1. This is for an Mw = 5.6 event in South Sumatra, recorded by station B01 at an epicentral distance of 120°. While all earthquakes with Mw > 5.0 in the GCMT catalog are discernible in the original vertical record, removing tilt and compliance noise makes them more visible and significantly increases their signal-to-noise ratio. This allows us to make Rayleigh wave amplitude and phase measurements on a larger number of events and also yields higher-quality measurements that are less biased by these sources of noise.

3. Two-plane-wave modeling

A total of 22 OBS stations are available to us. We will focus on 15 of them in this study (Fig. 2b), as the other seven stations appear to produce poor recordings, most likely due to a failure of the seismometer to correctly deploy and level on the seafloor. The compliance- and tilt-noise corrected vertical-component data are narrow-band passed and plotted on the screen for visual inspection. Each earthquake is examined independently.

Examples of recordings from two events that have been bandpassed and shifted according to group velocities of 3.8 km/s and 3.9 km/s, respectively, are shown in Fig. 2. While Event 1 produces almost identical traces across the array with fairly constant amplitudes along a wavefront, the waveforms from Event 2 are clearly affected by off-great-circle wave interference, as evident by the large variation of amplitudes along a wavefront.

To model the observed phases and amplitudes simultaneously, we follow the procedure described in Forsyth and Li (2005) and Harmon and Rychert (2016) and approximate the Rayleigh wave wavefield for a single event as an interference of two plane waves with 2-D finite frequency effects included (Yang and Forsyth, 2006; see Supplementary Materials Section 3). At each frequency, we use the inversion scheme described in Forsyth and Li (2005) to incorporate all events simultaneously to solve for the amplitudes, initial phases, and arrival angles of the two plane waves for each event, and the 2-D phase velocity variation, 1-D average azimuthal anisotropy, and 1-D average amplitude decay coefficient of the region. The error of each parameter is estimated by this inversion scheme. We also solve for an amplitude correction for each station to account for site effects. Since the azimuthal distribution of earthquakes is quite uniform (Figure S2) we do not perform any azimuthal normalization in our two-plane-wave modeling.

The total number of events used in the inversion scheme described above varies with frequency from 125 at 100 sec to 118 at 33 sec. Our preferred values of the Rayleigh wave amplitude decay coefficient and regionally averaged isotropic phase velocity are shown with the error bars in Fig. 3. Although damping and smoothing are needed when inverting for 2-D phase velocity maps, the effects of damping and smoothing on the regionally averaged phase velocity and decay rate are minor, compared to the estimated error from the inversion scheme. Similarly, the choice of the initial value of γ, the size of the area considered in the inversion, and whether extra terms are included to correct for site and station effects minimally affect the regionally averaged isotropic phase velocity and decay rate (Fig. 3).

4. 1-D shear-wave velocity and shear attenuation models

We use the Rayleigh wave amplitude decay coefficients and regionally averaged phase velocities to solve for 1-D models of shear-wave velocity and shear attenuation. The inversions are based on linearized perturbation theory
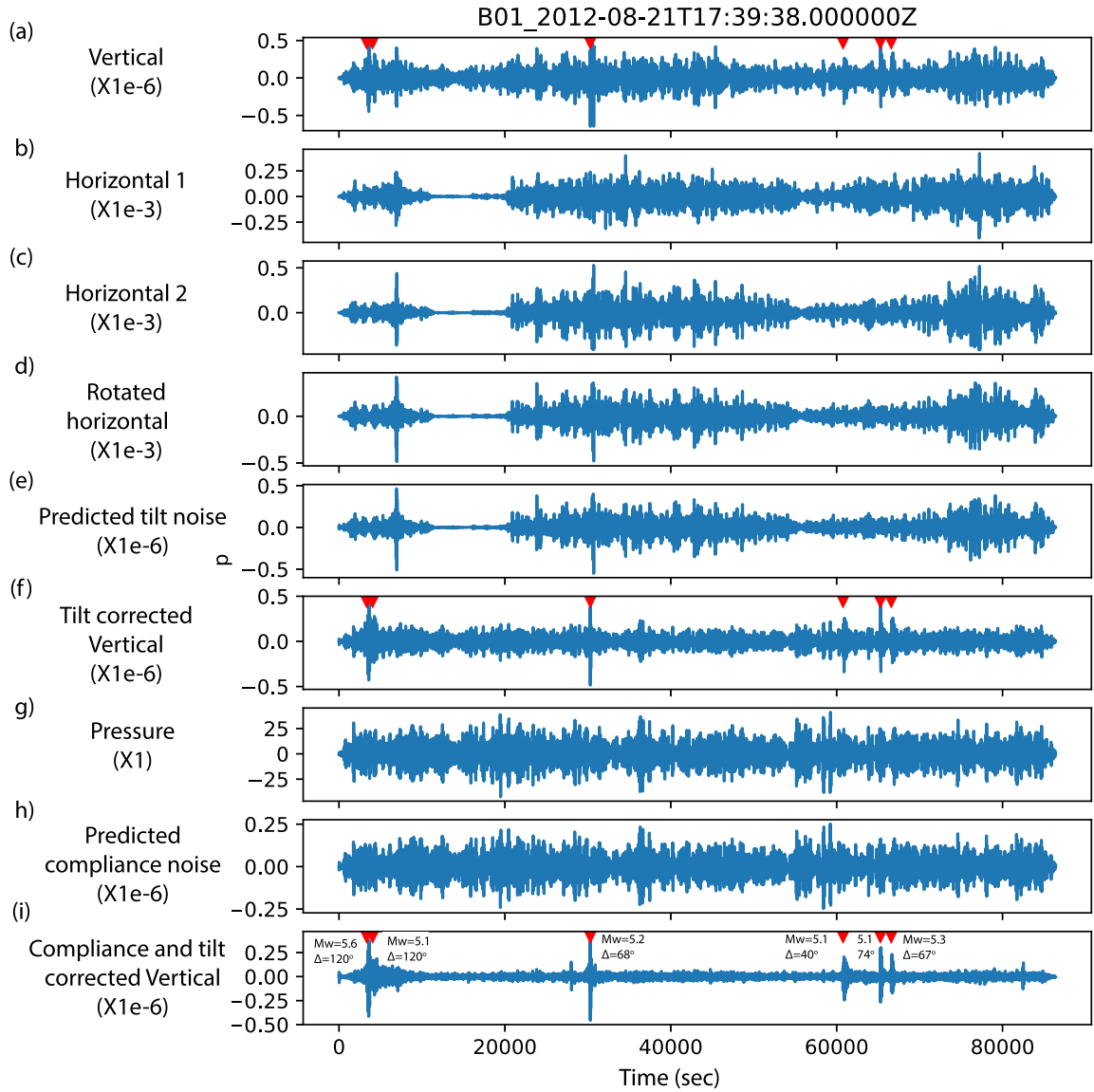
Fig. 1. Example of the effect of removing tilt and compliance noise for an event with origin time 2012-08-21 17:39:38, recorded by station B01. The units for seismic channels are meters and the unit for the pressure channel is kPa. All waveforms have been bandpass-filtered between 10 and 50 mHz. The upside-down triangles mark the six earthquakes with $M_W > 5$ in the GCMT catalog. The magnitudes and epicentral distances of these earthquakes are labeled in the bottom panel. (a) Vertical displacement from the original BHZ data after down-sampling and bandpass-filtering. (b) Same as (a), but for BH1. (c) Same as (a), but for BH2. (d) BH2 after rotation to have maximum coherence with the vertical in the absence of earthquake (see text for details). (e) Predicted tilt noise. (f) Tilt-corrected vertical record. (g) Record from the pressure gauge. (h) Predicted compliance noise. (i) Compliance- and tilt-corrected vertical record.

$$\delta c\left(\omega\right) = \int_0^a \left[K_{SV}\left(\omega, r\right) \delta V_{SV}\left(r\right) + K_{SH}\left(\omega, r\right) \delta V_{SH}\left(r\right) \right.$$
$$+ K_{PV}\left(\omega, r\right) \delta V_{PV}\left(r\right) + K_{PH}\left(\omega, r\right) \delta V_{PH}\left(r\right)$$
$$\left. + K_\eta\left(\omega, r\right) \delta\eta\left(r\right)\right] dr$$

$$Q^{-1}\left(\omega\right) = \int_0^a \left[K_{Q\mu}\left(\omega, r\right) Q_\mu^{-1}\left(r\right) + K_{Q\kappa}\left(\omega, r\right) Q_\kappa^{-1}\left(r\right)\right],$$

where $\delta c\left(\omega\right) = c\left(\omega\right) - c^{pre}\left(\omega\right)$ is the residual between observed and predicted isotropic phase velocity, and Rayleigh wave attenuation $Q^{-1}\left(\omega\right)$ is obtained from the amplitude decay coefficient using $\gamma\left(\omega\right) = \frac{\omega}{2U(\omega)} \frac{1}{Q(\omega)}$ where $U\left(\omega\right)$ is the group velocity at angular frequency ω. In these expressions, integration is from the center to the radius of the Earth a, V_{SV} and V_{SH} indicate the speeds of vertically and horizontally polarized, horizontally traveling shear waves, respectively, V_{PV} and V_{PH} indicate the speeds

of vertically and horizontally traveling compressional waves, and η is an anisotropic parameter that describes oblique propagation angles. Q_μ^{-1} and Q_κ^{-1} are shear and bulk attenuation. The sensitivity of the residual phase velocity or Rayleigh wave attenuation to each of these parameters is denoted by K with the appropriate subscript. The sensitivity kernels are calculated from the eigenfunctions of a reference 1-D Earth model. The model perturbations, such as $\delta V_{SV}\left(r\right)$, are expressed relative to the reference 1-D model, and the phase-velocity residual is expressed relative to the phase-velocity predictions of the reference 1-D model.

Fig. 4a compares our fundamental-mode Rayleigh wave phase velocity measurements with the 10-150 sec data of Lin et al. (2016); they are identical within uncertainty for the period band in which they overlap. Lin et al. (2016) used interstation cross-correlation to measure phase delays for 19 events and the Eikonal equation to determine phase-velocity maps; they use the phase-velocity value at the center of the array as the regionally averaged phase velocity. In contrast, we apply the two-plane-wave approach
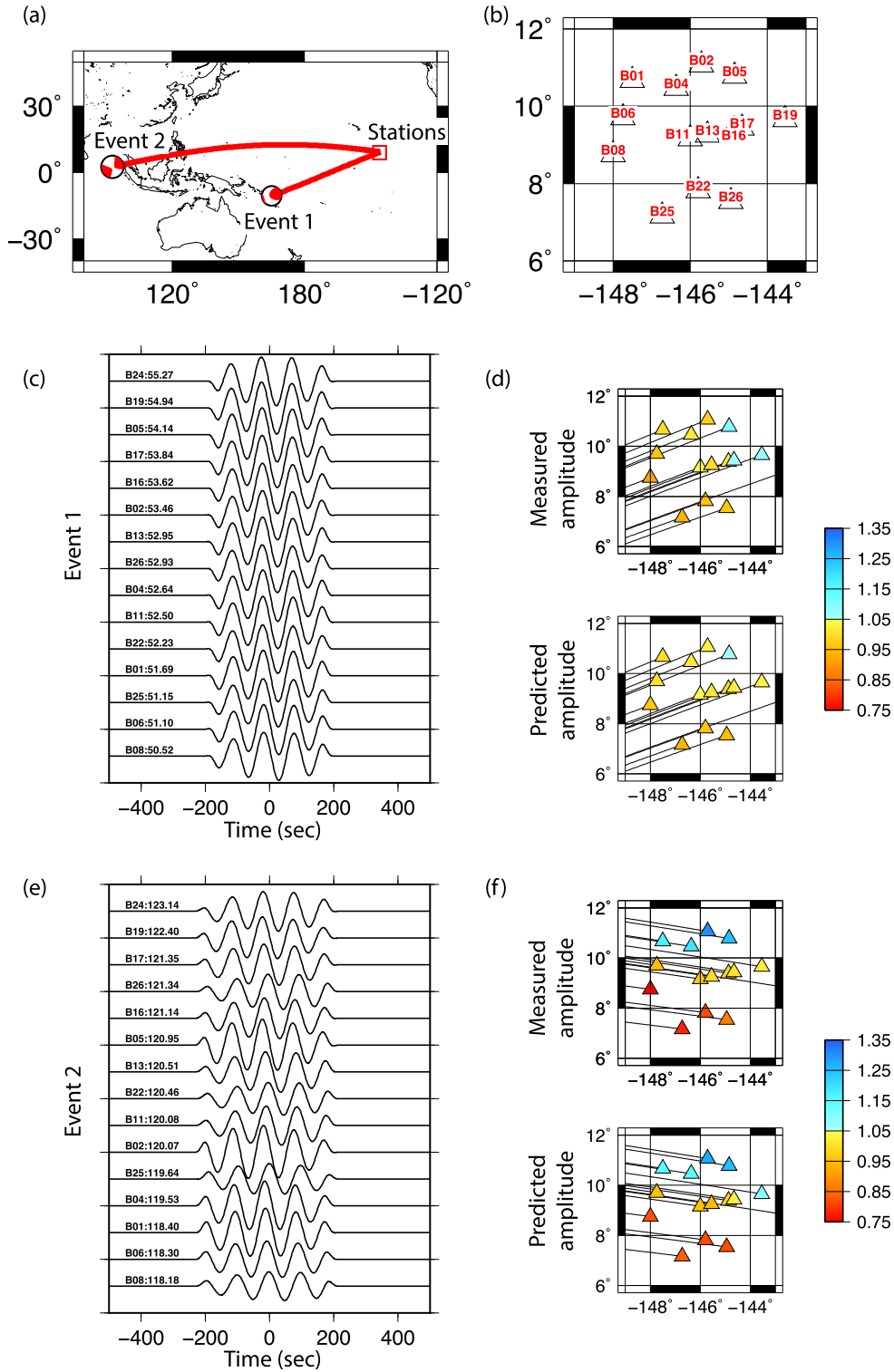
Fig. 2. Examples of waveforms and Rayleigh wave amplitudes. (a) Locations for Event 1 (2012-01-09 04:07:14) and Event 2 (2012-01-10 18:36:59). (b) Map of NoMelt stations used in this study. (c) Waveforms for Event 1, which have been corrected for compliance and tilt noise, bandpass-filtered around 100 sec, and windowed around the main wave train. A 1-D group velocity of 3.8 km/s is used to time-shift these waveforms. The station names and epicentral distances are labeled. For plotting purposes, waveforms have been normalized by their median amplitude. (d) Measured and predicted 100-sec amplitudes. Predicted amplitudes include the effects of two-plane wave interference, 1-D attenuation, and focusing-defocusing due to propagation through the elastic structure. The values plotted are the ratios of the amplitude at each station to the median value of the amplitudes measured at all stations. (e-f) same as (c-d), but for Event 2. A 1-D group velocity of 3.9 km/s is used for the time-shifting in (e). The large range (0.75-1.35) in panel (f) is mainly due to the effect of interference, which can shift the amplitude from its peak value to zero when the two plane waves are offset by half of a wavelength.

to more than 100 events to determine phase-velocity maps and use the average value in the study area as the regionally averaged phase velocity. The consistency between these two sets of values

suggests that they can be used with confidence. Fig. 4b shows two additional data sets measured by Russell et al. (2019) using ambient noise cross-correlation: the phase velocities of fundamental-
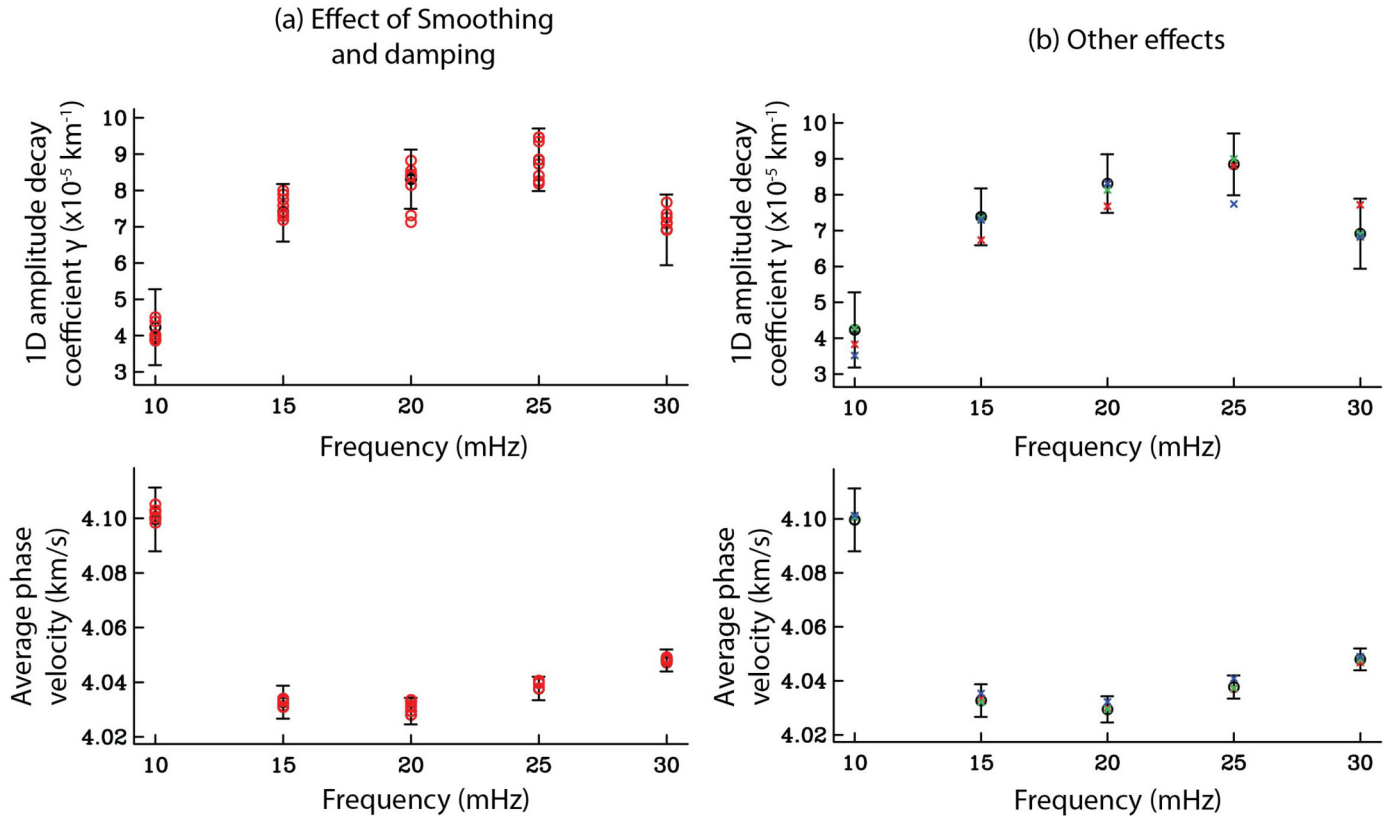
(a) Effect of Smoothing and damping

(b) Other effects

Fig. 3. Tests of the robustness of the 1-D amplitude decay coefficient (top) and regionally averaged phase velocity (bottom) estimated using the two-plane-wave approach. Black error bars are the preferred values, obtained from an inversion that uses a smoothness coefficient of 1.0 and a damping coefficient of 0.25. This inversion also includes station amplitude correction terms and uses a starting value $\gamma = 5 \times 10^{-5}$ and an inversion region that spans 150°W-140°W, 4.5°N-13.5°N. The average velocity is always calculated from the 2-D map in a region that spans 148°W-143°W, 7°N-11°N, where the ray path coverage is the densest. The error bars in velocity are determined by averaging the estimated error at each location in the 2-D region. Compared to calculating the error of the mean value, these are more representative of the actual errors in the inversion. (a) Effect of smoothing and damping on the estimated values (red circles). The smoothness coefficients tested are 0.1, 1.0 and 10.0. The damping coefficients tested are 0.025, 0.25 and 2.5. (b) Other effects on the estimated values: not including station terms (red crosses), using a different starting value $\gamma = 10 \times 10^{-5}$ (green crosses), and using a smaller inversion region which spans 149°W-142°W, 6.5°N-12.0°N (blue crosses). (For interpretation of the colors in the figure(s), the reader is referred to the web version of this article.)
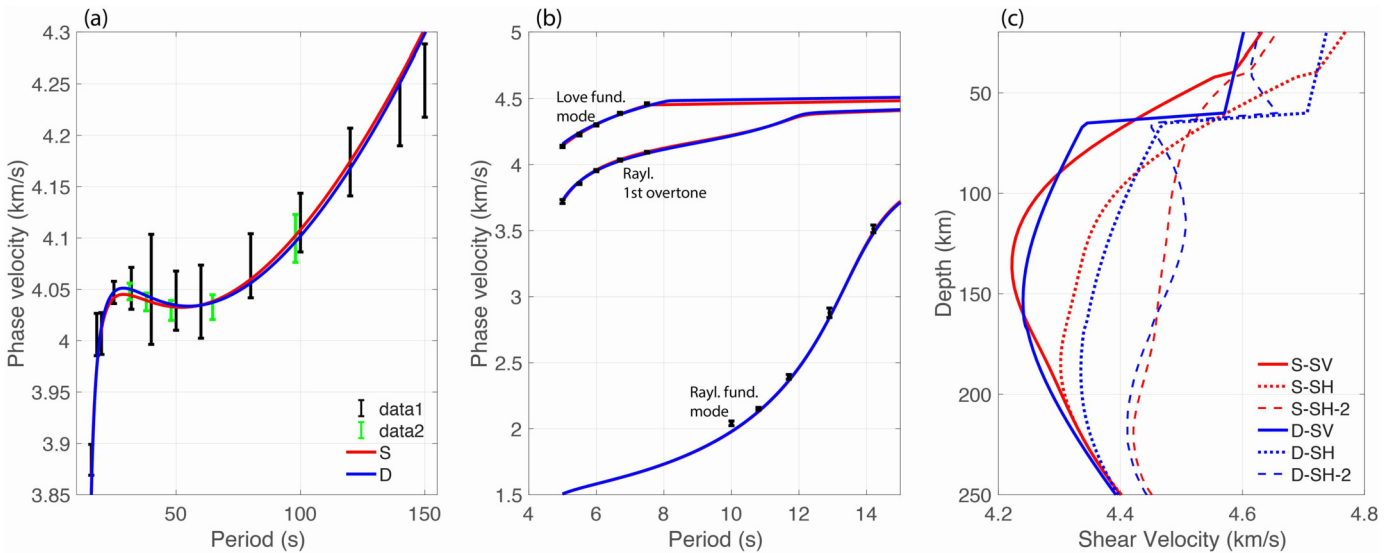

Fig. 4. (a) Fundamental-mode Rayleigh wave phase velocity. Black error bars (data1) show measurements from Lin et al. (2016). Green error bars (data2) are measurements from this study. Red curve shows predicted phase velocity using the smoothly varying final velocity model (S), and blue curve shows predictions for the final velocity model that contains a steep velocity reduction from 60-65 km (D). (b) Phase velocity measurements (error bars) and predictions from the final velocity models (red and blue curves) for fundamental-mode Rayleigh and Love waves and first-overtone Rayleigh waves (Russell et al., 2019). (c) Vertically (SV) and horizontally (SH) polarized shear velocity for the smooth (S) and discontinuous (D) final velocity models. Also shown are the V_{SH} profiles (SH-2) if the strength of radial anisotropy (V_{SH}-V_{SV}) is fixed to its value at the NoMelt location in the SEMum2 global velocity model (French et al., 2013).
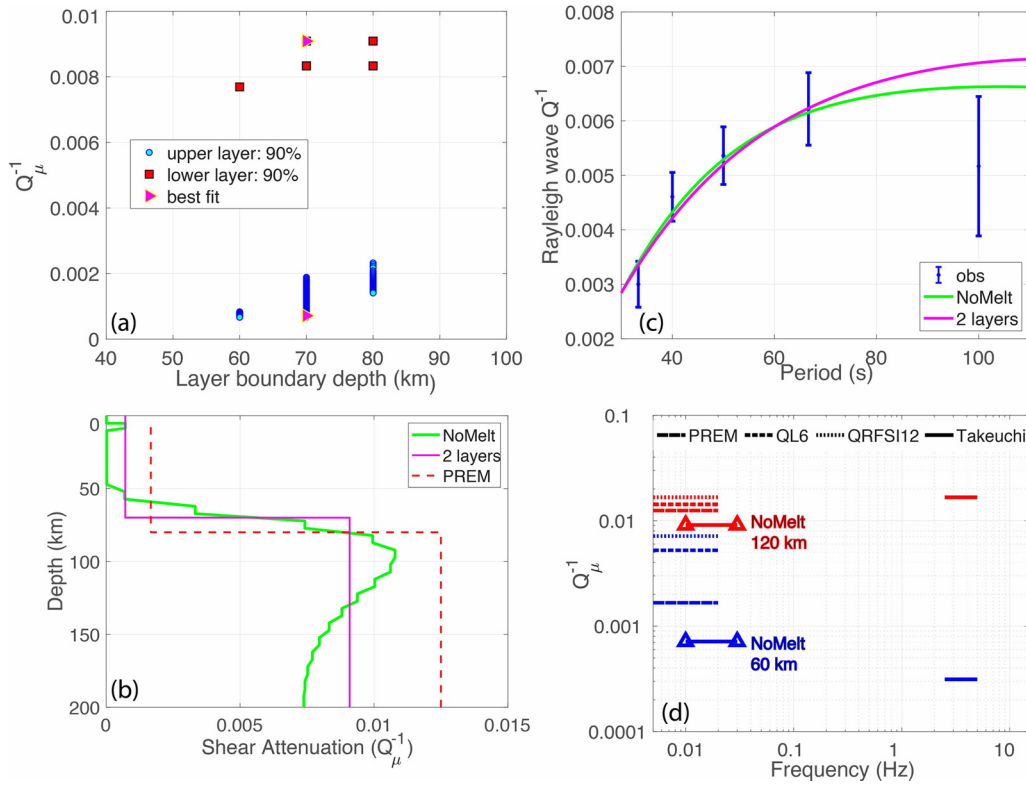
Fig. 5. Attenuation results. (a) Grid search for a two-layer Q_μ model. We test Q_μ from 50 to 1500 in increments of 10 and depth of the layer boundary from 0 to 400 km in increments of 10 km. Symbols show 193 acceptable models (90% confidence level, with misfit $\chi^2 \leq 4.6$): blue circles for the shallow layer and red squares for the deeper layer. Magenta triangles are the lowest-misfit model. (b) The final attenuation model (green) is compared to PREM and the best-fitting two-layer model from the grid search. (c) Blue error bars show Rayleigh wave attenuation measured in the NoMelt area. Green curve is the prediction of the final model and the magenta curve is the prediction of the two-layer model. (d) Implications for frequency dependence of attenuation in the lithosphere (blue; ~60 km) and asthenosphere (red; ~120 km). The NoMelt results are compared to previous low-frequency shear attenuation values from global 1-D models PREM and QL6 (Durek and Ekström, 1996) and 3-D model QRFSI12 (Dalton et al., 2008) in the NoMelt region and the high-frequency result in the northwestern Pacific from Takeuchi et al. (2017). In contrast to the earlier studies, low attenuation in the NoMelt lithosphere suggests weak or no frequency dependence of attenuation in both layers.

mode Love waves and first-overtone Rayleigh waves in the period range 5-7.5 sec.

Because of the similarities described above, in our velocity inversion, which solves for $\delta V_{SV}(r)$ and $\delta V_{SH}(r)$, we use the three data sets of Lin et al. (2016) and Russell et al. (2019) as these data sets cover a larger frequency range compared to the data set obtained with two-plane-wave modeling. Details of the velocity inversion can be found in Russell et al. (2019). The Love wave data provide constraints on V_{SH} in the shallow mantle, as discussed further in Section 5.2, and the overtone Rayleigh wave data improve constraints on V_{SV} at depths up to 15-20 km deeper than the Moho. The Love wave data were obtained from ambient noise in a short-period band where fundamental-mode group and phase velocity are well separated from those predicted for higher modes (Russell et al., 2019), suggesting that bias from overtone interference (e.g., Foster et al., 2014) is not a significant source of error.

We repeat the velocity inversion using two different reference models, one that contains smoothly varying velocity in the mantle and one that contains a 5% velocity reduction from 60 km to 65 km in depth. A velocity reduction of this magnitude in this depth range is supported by the S-to-p receiver function study at NoMelt stations by Mark et al. (2019) and is consistent with earlier studies of scattered waves in the Pacific (Kawakatsu et al., 2009; Rychert and Shearer, 2011; Schmerr, 2012). Since the broad depth sensitivity kernels of surface waves prevent us from being able to resolve such a strong contrast with depth even if it exists, we must impose it via the reference model. The two final velocity models (Fig. 4c) make nearly identical predictions of phase velocity and fit all data sets equally well (Figs. 4a,b).

Unlike Russell et al. (2019) and most other seismic models, we do not correct for the effects of anelastic physical dispersion. Inherent in these corrections are assumptions about the frequency dependence of attenuation and the relationship between attenuation and velocity (e.g., Liu et al., 1976) that may not be appropriate for the upper mantle and that complicate efforts to compare seismic models to laboratory experiments of the effects of anelasticity. Thus, our new NoMelt velocity models (Fig. 4c) are not defined at a particular reference frequency, and instead we consider the relevant frequency at each depth to be the frequency of the Rayleigh wave that is most sensitive to that depth. We note that not correcting the phase velocities for anelastic physical dispersion could be problematic if observations from very different periods were being used to constrain velocity structure at the same depth. However, the depth range of sensitivity for the fundamental-mode and first-overtone Rayleigh waves used in this study only overlaps at depths <25 km; at greater depths the velocity structure should not be affected by neglecting the difference in frequency content.

The attenuation inversion considers only shear attenuation Q_μ^{-1}, since both bulk attenuation Q_κ^{-1} and the sensitivity of Rayleigh wave attenuation to bulk attenuation, $K_{Q_\kappa}(\omega, r)$, are small (e.g., Durek and Ekström, 1996). The smoothly varying final velocity model (Fig. 4c) is used to calculate sensitivity to shear attenuation $K_{Q_\mu}(\omega, r)$ and the group velocity $U(\omega)$. The inversion for shear attenuation occurs in two steps. We first perform a grid search to identify a good starting model. We found that a model with two layers, where the free parameters are shear attenuation in the upper and lower layers and the transition depth between them, is sufficient to explain our data (Fig. 5a,c). The two-layer model with
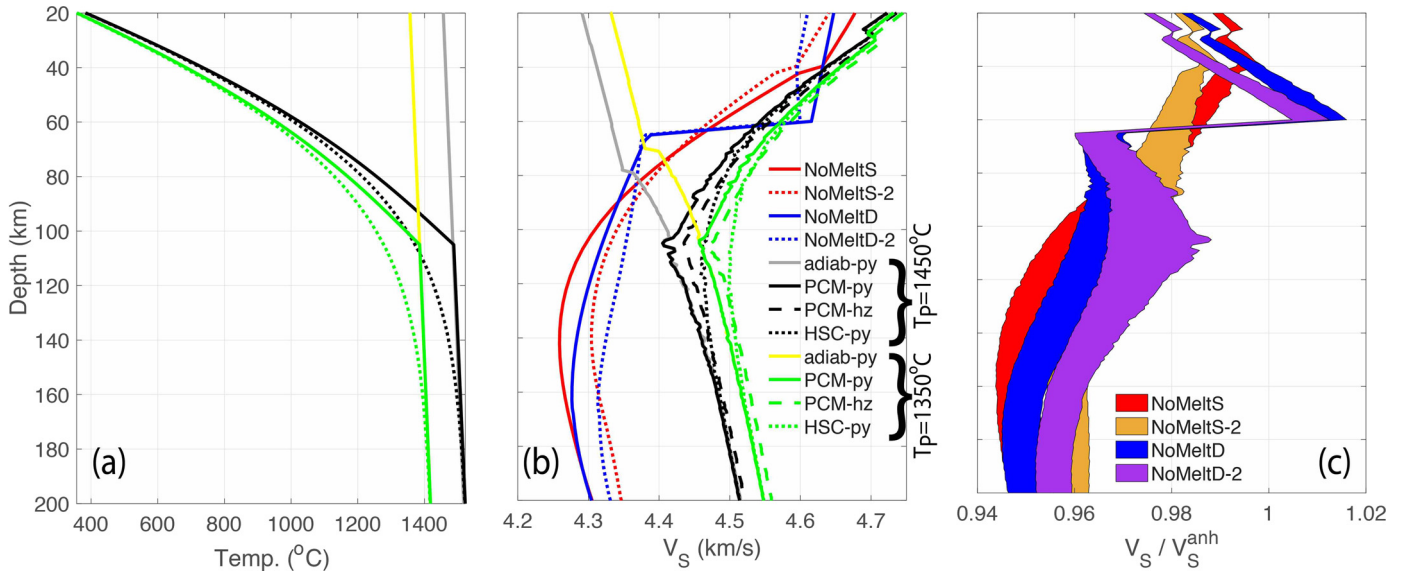
Fig. 6. Isolating the anelastic contribution to V_S. (a) Temperature profiles calculated for half-space cooling models (dotted) and plate cooling models with plate thickness = 105 km (solid) that join mantle adiabats with potential temperatures of 1350 °C (green) and 1450 °C (black). Yellow and gray curves show extension of the adiabats to the surface. (b) Predicted isotropic (Voigt averaged) anharmonic shear velocity for the temperature profiles in (a) using Perple_X with the thermodynamic data, solution models, and shear moduli of Stixrude and Lithgow-Bertelloni (2011). Calculations using pyrolite (py) and harzburgite (hz) compositions are shown. Red and blue curves show Voigt-averaged V_S from the smooth (NoMeltS) and discontinuous (NoMeltD) final velocity models (Fig. 4c). Solid and dotted NoMelt curves are based on different assumptions about V_{SH}; see text for details. (c) Ratio of the NoMelt Voigt-averaged V_S models to the Perple_X-predicted anharmonic V_S profiles. Colored fields enclose the minimum and maximum values at each depth.

the smallest misfit has $Q_\mu = 1400$ in the upper layer, $Q_\mu = 110$ in the lower layer, and a transition depth of 70 km. We have also performed a parameter search for suitable three-layer models (Supplementary Materials Section 3). But given that we only have five attenuation measurements, the details of these three-layer models are hard to constrain, and we do not interpret them in this paper.

We then perform a full depth inversion using the best-fitting two-layer model as the starting model with respect to which we solve for perturbations. A small amount of smoothing and damping is applied to ensure stability. The resulting attenuation model (Fig. 5b) contains a shallow layer of very low attenuation that is underlain by moderate attenuation, with a fairly abrupt transition that occurs between 60 km and 80 km. At depths 80-130 km, attenuation is slightly higher ($Q_\mu = 92 - 110$) than in the two-layer model, and at depths 130-200 km it is slightly lower ($Q_\mu = 110 - 135$). Fig. 5c shows that both the two-layer and depth-dependent models fit the data within uncertainty.

5. Discussion

5.1. Comparison to other studies

The first observation in our study is that attenuation ($1/Q_\mu$) in the shallow part of the mantle (<70 km, $Q_\mu \sim 1400$) is lower than the value in PREM ($Q_\mu \sim 600$; Dziewonski and Anderson, 1981) and much lower than the value in the NoMelt region determined from the global attenuation model QRFSI12 ($Q_\mu \sim 140$; Dalton et al., 2008). In contrast, attenuation at greater depths (>70 km, $Q_\mu \sim 110$) is only slightly lower than the value in PREM ($Q_\mu \sim 80$) and considerably lower than in QRFSI12 ($Q_\mu \sim 60$). For another comparison, using the same two-plane-wave approach as our study, Yang et al. (2007) reported values of Q_μ of ~ 79 and ~ 98 for young oceanic mantle in the depth range 55 to 125 km in the MELT and GLIMPSE experiments near the East Pacific Rise, and Ruan et al. (2018) found $Q_\mu \sim 76$ in the depth range 90 to 170 km and ~ 128 in the depth range 150 to 300 km beneath the Juan de Fuca plate area. Unlike the NoMelt area, the western side

of the spreading centers in both of these areas of young seafloor have abundant seamounts that have been attributed to hotspot influence (Desonie and Duncan, 1990) that could be responsible for the slightly higher attenuation. We emphasize that all of these models are constrained by seismic signals in roughly the same period range (~ 25-100 sec). Thus, differences between the global and regional studies reflect the fact that while large-scale attenuation structure can be robustly obtained in global studies (Dalton et al., 2008; 2017), both the coarseness of the model parameterization and the use of long paths obscure details of structure that are better imaged by regional seismic arrays.

At higher frequency (~ 3 Hz), Takeuchi et al. (2017) found that beneath old seafloor in the western Pacific the intrinsic Q_μ is ~ 3200 in the lithosphere and ~ 60 in the asthenosphere. They suggested that differences exist in the frequency dependence of attenuation in these two layers on the basis of comparison to the low-frequency Q_μ values from QRFSI12, with stronger frequency dependence in the lithosphere and frequency independence in the asthenosphere. In contrast, the results of our study – notably the very low attenuation at shallow depths – indicate weak frequency dependence in both layers (Fig. 5d).

5.2. Effect of anelasticity on shear velocity

Fig. 6 shows how we estimate the effect of anelasticity on shear velocity. We consider a range of temperature profiles appropriate for 70-Myr seafloor (Fig. 6a), including half-space cooling and the plate cooling model (e.g., Stein and Stein, 1992). We use the Perple_X software (Connolly, 2009) to compute isotropic shear velocity for compositions corresponding to pyrolite and harzburgite (Table 1). These calculations utilize the thermodynamic data and solution models of Stixrude and Lithgow-Bertelloni (2011). The resulting elastic-velocity profiles (Fig. 6b) show that velocity decreases with depth within the thermal boundary layer and increases slightly with depth along the mantle adiabat; the low-velocity zone reaches its minimum at the depth where the conductive layer merges with the adiabat. As expected, velocities calculated for the temperature profiles that merge with the hotter

Table 1
Major-element compositions for pyrolite and harzburgite.

(wt. %)	pyrolite	harzburgite
SiO_2	45.36	45.18
Al_2O_3	4.49	4.42
FeO	8.11	7.63
MgO	38.10	38.96
CaO	3.58	3.41
Na_2O	0.36	0.40

adiabat (potential temperature $T_P = 1450\,°C$) are offset to lower values relative to those calculated for the colder adiabat. The effect of composition is relatively minor; the more depleted harzburgite composition yields slightly higher velocities at a given temperature and pressure, but temperature variations have a bigger effect.

Since the Perple_X velocities are purely elastic (anharmonic), the effects of anelasticity in the upper mantle can be deduced by comparing the NoMelt velocity model to them (Figs. 6b,c). NoMelt V_{SV} is well constrained to a depth of ~300 km, but V_{SH} is constrained only in the crust and the upper 25 km of the mantle. We therefore consider two different approaches in order to estimate V_{SH} at greater depth. One, in developing the two final NoMelt velocity models (NoMeltS and NoMeltD), we assume that the magnitude of radial anisotropy in the lithosphere (~3%) remains constant through the low-velocity zone and tapers out in the depth range 200-250 km, which is generally consistent with previous regional estimates (e.g., Nishimura and Forsyth, 1989; Gaherty et al., 1996). Two, we fix the magnitude of radial anisotropy V_{SH}-V_{SV} at its value in the global velocity model SEMum2 (French et al., 2013) as sampled at the NoMelt location and estimate V_{SH} by adding this value to the well constrained NoMelt V_{SV} profile. The second approach, labeled NoMeltS-2 and NoMeltD-2, yields higher V_{SH} (Fig. 4c) and therefore higher isotropic V_S at depths >~75 km (Fig. 6b). The use of radial anisotropy from SEMum2 is meant to explore the extent to which our results depend on assumptions about V_{SH}.

Fig. 6c shows that the effects of anelastic relaxation on shear velocity are largest at depths >70 km, where they can be >5% depending on which NoMelt and anharmonic velocity profiles are used. Since the scattered-wave analysis provides evidence of a sharp velocity gradient in the shallow mantle (Mark et al., 2019), we focus on the NoMeltD models in subsequent interpretation.

Fig. 6b shows that anelasticity may cause the low-velocity zone to occur at a larger depth than that at which the conductive layer and the adiabat merge, which could complicate efforts to infer, for example, thermal structure from shear velocity models if the anelastic effect is not properly accounted for. This apparent deepening of the low-velocity zone could provide an important observational constraint on the activation volume for the dissipative processes that are responsible for attenuation, including transient creep. However, we note that the vertical averaging or smearing inherent in surface-wave inversions can also deepen the apparent velocity minimum, especially given the steep velocity gradient predicted within the thermal boundary layer.

5.3. Implications for anelasticity in the lithosphere and asthenosphere

Anelastic behavior in fine-grained polycrystalline materials is typically attributed to sliding along grain boundaries (e.g., Gribb and Cooper, 1998; Cooper, 2002). The application of an external shear stress causes an instantaneous elastic strain followed by sliding along the boundaries between individual grains. Initially the sliding is accommodated by elastic distortions of the grains, resulting in stress concentrations at the grain corners, which act as a restoring force that allows for gradual recovery of the strain once the external stress is removed (Gribb and Cooper, 1998). This

process is called elastically accommodated grain-boundary sliding (EAGBS), and its characteristic time scale is $\tau_e = \eta_{gb}d/\mu_U\delta$, where η_{gb} and δ are the viscosity and thickness of the grain boundary, respectively, d is the grain size, and μ_U is the unrelaxed shear modulus.

With continued application of the external stress, diffusion of matter along the grain boundaries facilitates evolution of the stress states towards the configuration required for steady-state creep. This process is referred to as diffusionally accommodated grain-boundary sliding (DAGBS), which, for the steady-state process is termed Coble creep or, more generally, diffusion creep. When the external stress is removed, the steady-state stress configuration is relieved via diffusion, allowing for gradual recovery. DAGBS has a duration τ_d that is similar to the Maxwell relaxation time $\tau_M = \eta_{ss}/\mu_U$, where $\eta_{ss} >> \eta_{gb}$ is the viscosity associated with steady-state creep. Using $\mu_U = 75$ GPa, $\eta_{ss} = 10^{20}$ Pa-s, and $d = 10^{-2}$ m, and assuming $\eta_{gb} = 10^6$ Pa-s and $\delta = 10^{-9}$ m (e.g., Sundberg and Cooper, 2010), τ_d is roughly seven orders of magnitude larger than τ_e.

In terms of an attenuation spectrum, EAGBS manifests as an attenuation peak centered at frequency $1/\tau_e$ ($= f_e$), and DAGBS persists throughout a broad frequency range and manifests as a mild frequency dependence of attenuation, $Q^{-1} \sim f^{-(0.25-0.35)}$ (Gribb and Cooper, 1998). This latter phenomenon, often referred to as the high-temperature background (HTB) or the absorption band, is consistently detected and characterized in experimental studies of attenuation in olivine, olivine-orthopyroxene, and borneol (e.g., Jackson and Faul, 2010; Sundberg and Cooper, 2010; Yamauchi and Takei, 2016). However, experimental evidence of a peak associated with EAGBS is more variable. For example, Sundberg and Cooper (2010) showed that fitting both their modulus and attenuation measurements on peridotite samples (melt content = 1.5%) required an EAGBS peak. Jackson et al. (2004) and Faul et al. (2004) showed that the attenuation spectra of their experiments on melt-bearing olivine samples can be described as a dissipation peak superimposed on the HTB. Although those authors attributed the peak to EAGBS, subsequent high-resolution imaging of wetted grain boundaries has shown that melt squirt rather than EAGBS may be responsible for the peak observed in melt-bearing samples (Garapic et al., 2013; Faul and Jackson, 2015). In their experiments on borneol, Yamauchi and Takei (2016) showed that a high-frequency peak exists in melt-free samples and grows wider and moves to lower frequency as the temperature of the experiments approaches the solidus; those authors argued for a diffusional mechanism to explain the peaks in their data instead of EAGBS.

Attenuation measurements on melt-free olivine samples suggest but do not definitively show evidence of a peak associated with EAGBS (Jackson and Faul, 2010; Jackson et al., 2014). The measurements hint that the peak appears at relatively short periods, low temperatures, and large grain sizes (i.e., approaching the elastic regime), and models that allow for both the HTB and the EAGBS peak are better able to fit the data than those that contain only the HTB. However, as described by Jackson et al. (2014), the experimental challenge is that the steel material used as a jacket around the olivine sample undergoes a phase transition and associated change in mechanical behavior in the same temperature range (700-900 °C) in which the measurements suggest a peak, making it difficult to isolate the viscoelastic effects of olivine from those of the jacket. When Jackson et al. (2014) repeated one experiment with olivine in a copper jacket instead of steel the results were also suggestive of a broad dissipation peak, but Jackson et al. (2014) caution that the evidence thus far is circumstantial and additional tests are needed.

Laboratory measurements of attenuation in olivine with elevated water content (i.e., with hydrogen-related defects) are es-
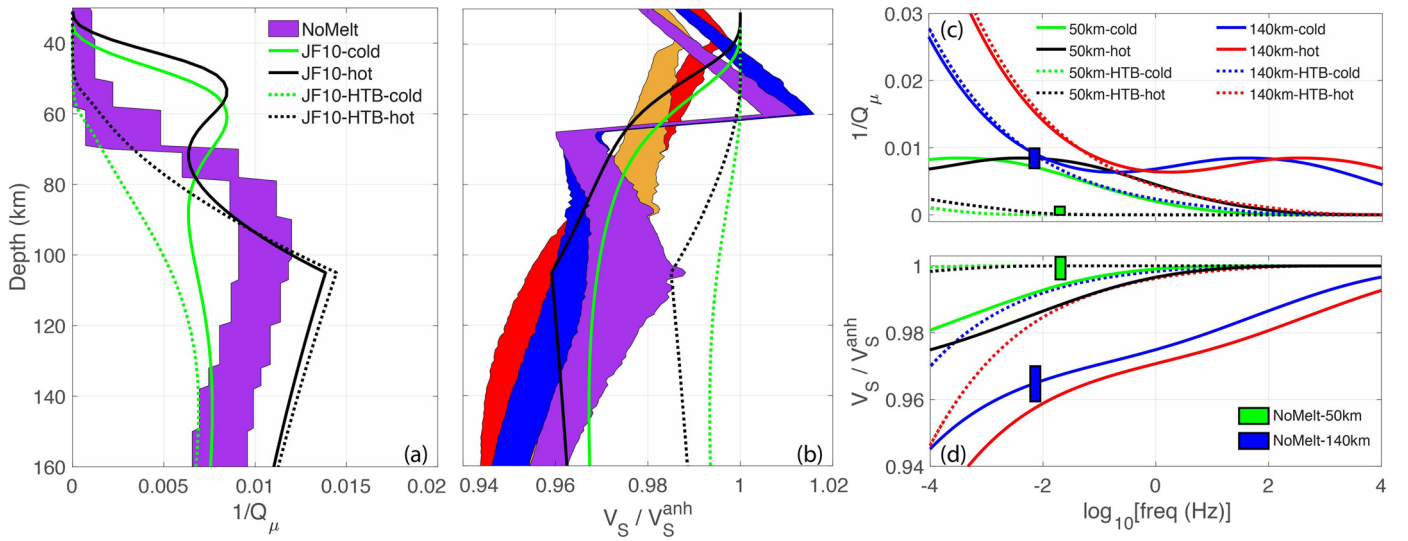
Fig. 7. (a) Depth profiles of shear attenuation. The field of values determined for NoMelt (Fig. 5b) is compared to predictions of the Jackson and Faul (2010) parameterization for grain size = 10 mm. Curves labeled "cold" and "hot" refer to the calculations performed using the half-space cooling geotherm with potential temperature = 1350 °C and the plate-cooling geotherm with potential temperature = 1450 °C, respectively (Fig. 6a). For curves labeled "HTB", the terms in the JF10 parameterization that correspond to the EAGBS peak have been excluded from the calculation. (b) As in (a) but for the predicted and NoMelt shear-velocity reduction. See Fig. 6c for reference to colors. (c,d) Predicted spectra of attenuation and shear-velocity reduction for depths of 50 and 140 km. The green and blue boxes enclose the range of NoMelt values; the NoMeltD-2 V_S model is used in (d).

pecially challenging, and consequently only two such studies have been published (Aizawa et al., 2008; Cline et al., 2018). While Cline et al. (2018) found that the influence of water on attenuation is small, Karato and Park (2019) argued that it is difficult to reconcile this result with experimental studies showing that water enhances steady-state diffusion creep (e.g., Mei and Kohlstedt, 2000). Furthermore, in a series of papers Karato and colleagues have proposed that water should increase the frequency of the EAGBS peak by several orders of magnitude relative to the water-free scenario (Karato, 2012; Olugboji et al., 2013; Karato and Park, 2019).

An important distinction between the HTB and EAGBS anelastic mechanisms is their effect on shear modulus. While the HTB causes a mild frequency dependence of shear modulus, EAGBS can introduce a strong frequency dependence in the vicinity of the peak. Notably, the modulus is lower ("relaxed") at frequencies less than that of the EAGBS peak whereas the modulus is high and close to its purely elastic value ("unrelaxed") at frequencies higher than the peak. The magnitude of the modulus reduction due to EAGBS depends only on Poisson's ratio (e.g., Sundberg and Cooper, 2010), and the sharpness of the modulus change with frequency depends on the width of the EAGBS peak in frequency (e.g., Olugboji et al., 2013). In the model of Karato (2012), if the EAGBS peak shifts from a relatively low frequency in dehydrated mantle to high frequency in hydrated mantle, seismic waves could sample the unrelaxed modulus in the dehydrated mantle and the relaxed modulus in the hydrated mantle. As a result, a sharp hydration boundary with depth could manifest as a discontinuity in shear velocity.

Here, we use the NoMelt shear attenuation and velocity models to investigate the contributions of the HTB and EAGBS in the Pacific upper mantle. Fig. 7a,b compares the NoMelt Q_μ and V_S ranges to predictions of the anelastic parameterization of Jackson and Faul (2010), hereinafter JF10, which is based on their experiments on melt-free olivine samples. The predictions are shown for grain size = 10 mm and the coldest and hottest geotherms in Fig. 6a. The JF10 Q_μ predictions bracket the NoMelt range at depths >~90 km, but at 40-80 km the JF10 parameterization predicts much higher attenuation than observed. The JF10 V_S predictions match the NoMelt range reasonably well for depths 80-120 km. At depths <60 km the JF10 predictions are generally slower

than the NoMeltD models, and at depths >120 km the predictions overlap with but tend to be somewhat faster than the NoMelt models. In Supplementary Materials Section 4 we show a comparison to the anelastic parameterization of Yamauchi and Takei (2016). We focus our subsequent analysis on the JF10 parameterization.

In the JF10 parameterization, the frequency of the EAGBS peak depends on temperature, pressure, and grain size. Given a grain size of 10 mm and reasonable temperature estimates for 70-Myr lithosphere, the frequency of the peak in the JF10 parameterization is ~0.01 Hz at 50-km depth and ~100 Hz at 140-km depth (Fig. 7c). As a result, the attenuation of the 36-sec (0.028 Hz) Rayleigh waves that are most sensitive to 50-km depth is due mostly to the EAGBS peak, whereas the attenuation of the 100-sec (0.01 Hz) waves that are most sensitive to 140-km depth is due mostly to the HTB (Fig. 7c) in the JF10 parameterization. We assume period (s) = depth (m)/1400 for Rayleigh wave depth sensitivity (Forsyth, 1992). In Fig. 7c,d, we illustrate the relative contributions of the HTB and the EAGBS peak to shear attenuation and velocity. At 50 km, HTB yields little attenuation and nearly elastic velocity as a result of the cold temperatures; HTB produces higher attenuation and a moderate velocity reduction under the warm conditions expected at 140 km. The effect of the EAGBS peak can be understood by comparing the solid and dashed curves in Fig. 7d. As described above, shear velocity is significantly reduced at frequencies less than that of the EAGBS peak.

The comparison of observations and the JF10 predictions in Fig. 7 suggests that shear attenuation and velocity at depths <70 km are better fit by the HTB only whereas the EAGBS peak is needed in addition to the HTB to explain the low shear velocities at depths >70 km (Fig. 7a,b). Since Jackson and Faul (2010) and Jackson et al. (2014) caution that there is uncertainty in the details of the EAGBS peak resolved by their experiments, in Fig. 8 we search for the peak frequency that best matches the NoMelt shear attenuation and velocity values simultaneously. In other words, we abandon the dependence of the JF10 peak frequency on temperature, pressure, and grain size and instead test many different peak frequencies. We retain the amplitude and width of the peak as prescribed by the JF10 parameterization but allow its frequency to vary. Future work will explore how variations in all aspects
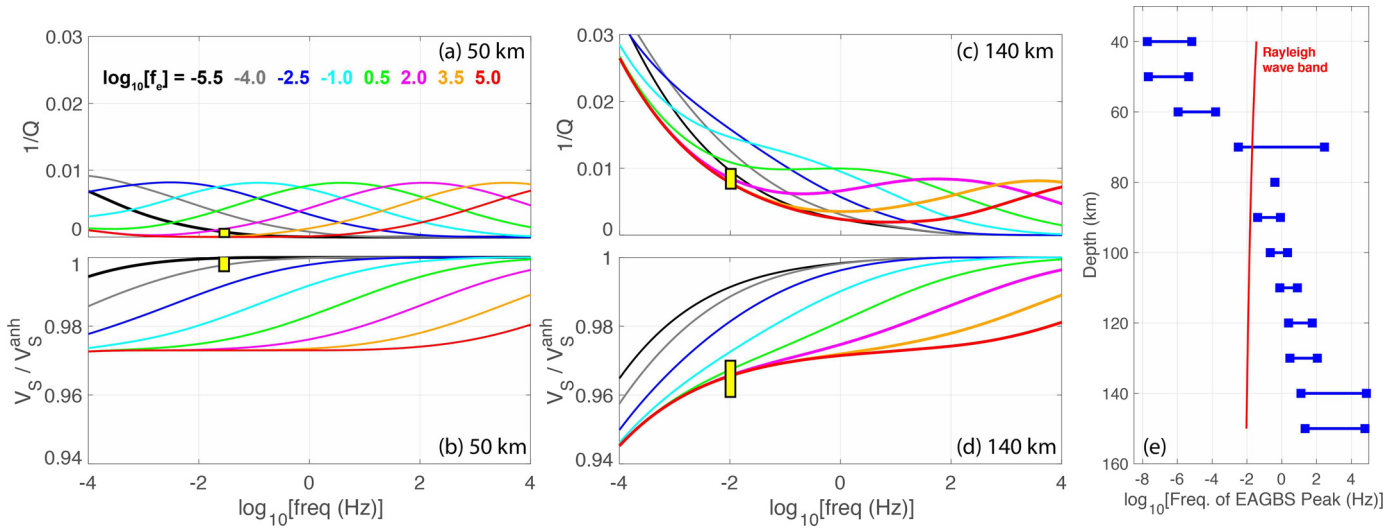
Fig. 8. (a,b) Predicted spectra of attenuation and shear-velocity reduction. All spectra have the HTB corresponding to depth = 50 km and temperature = 818 °C, but the eight examples have different values for the center frequency (f_e) of the peak commonly attributed to elastically accommodated grain boundary sliding, as labeled in (a). The small yellow boxes enclose the range of NoMelt values; the NoMeltD-2 V_S model is shown here. 36-sec Rayleigh waves have their peak sensitivity at 50 km. Spectra that fit both NoMelt attenuation and velocity are drawn with a thicker line. (c,d) As in (a,b) but for depth = 140 km, temperature = 1373 °C, and relevant period = 100 sec. (e) At each depth the blue bar spans the range of EAGBS peak center frequencies that fits the NoMelt attenuation and NoMeltD-2 V_S values simultaneously. Red line shows the frequency of the Rayleigh wave most sensitive to each depth. When the EAGBS peak frequency is higher (lower) than the Rayleigh wave frequency, the Rayleigh waves sample the relaxed (unrelaxed) shear modulus.

of the peak (shape, amplitude, frequency) affect attenuation and velocity; here we focus on the effects of the peak frequency. On the other hand, since the HTB and its dependence on temperature, frequency, and grain size are well characterized by laboratory experiments, we use the expressions and parameters for the HTB and viscous contributions to the real and imaginary parts of the dynamic compliance function exactly as given by Jackson and Faul (2010). Our approach of superimposing two creep functions (and their frequency spectra) is modeled after the work of Sundberg and Cooper (2010).

Fig. 8a,b provides examples of our approach for depth = 50 km. Eight examples of the frequency dependence of attenuation and shear velocity are shown; the HTB and viscous parameters are the same in all eight and predicted from the Jackson and Faul (2010) expressions assuming temperature = 818 °C and grain size = 10 mm. At these conditions the predicted attenuation and velocity reduction from HTB alone are tiny. The position of the EAGBS peak in frequency varies between the eight examples, from $10^{-5.5}$ Hz (31,623 sec) to $10^{5.0}$ Hz. Since the HTB contribution to attenuation is so small, the EAGBS peak is the dominant feature in the attenuation spectra. It is also the dominant factor in the shape of the velocity spectra (Fig. 8b). When the EAGBS peak is positioned at low frequency, the unrelaxed modulus (and thus high velocity) is present throughout most of the frequency range considered. When the EAGBS peak is at high frequency (orange, red), the relaxed modulus (low velocity) persists throughout most of the frequency range. Because the HTB has little effect on shear velocity, all examples approach the same minimum velocity, which is dictated by the Poisson's ratio of olivine.

Fig. 8c,d shows the attenuation and velocity spectra at depth = 140 km. The HTB and viscous parameters are the same for all eight examples; we assume temperature = 1373 °C and grain size = 10 mm. Under these conditions the HTB contribution is significant; its effect on attenuation is most visible at low frequencies for the examples in which the EAGBS peak is positioned at high frequency (orange, red) and does not overlap with the HTB. The presence of the EAGBS peak elevates attenuation above its HTB value in the relevant frequency range. As expected, the EAGBS peak modifies the frequency dependence of shear velocity and allows the relaxed

velocity to exist throughout a broader frequency range when the EAGBS peak is located at high frequency.

By requiring the NoMelt attenuation and velocity values to be fit simultaneously, we can determine the frequency range for the EAGBS peak that is allowed by the seismic models. For example, in Figs. 8a,b, the very low attenuation and high velocity at 50-km depth require that the modulus is nearly unrelaxed and that the attenuation peak is displaced from the seismic frequency, which we assume is 0.028 Hz (36 sec). These conditions can be met if the peak frequency is very low, between $10^{-7.67}$ and $10^{-5.35}$ Hz, or if there is no EAGBS peak at 50 km. In contrast, at 140-km depth, the moderate attenuation and very low velocity require that the modulus is relaxed and that the attenuation peak is displaced from the seismic frequency (0.01 Hz), which is possible if the peak frequency is $> 10^{1.1}$ Hz.

In practice we search 125 attenuation and velocity spectra at each depth and identify all that can fit both velocity and attenuation. Fig. 8e summarizes the results as applied to the discontinuous final velocity model with radial anisotropy assumed to be the same strength as at the NoMelt location in SEMum2 (French et al., 2013), which is labeled as NoMeltD-2 in Fig. 6c; for shear attenuation, the range of values from the two-layer and final models is used. Furthermore, for the results in Fig. 8e the HTB is calculated using grain size = 10 mm and temperature estimated from half-space cooling with potential temperature = 1350 °C (Fig. 6a). We repeated our approach with warmer temperatures (e.g., the plate-cooling model with potential temperature = 1450 °C) but found little success, mostly because the HTB under these conditions predicts higher attenuation than measured at NoMelt.

We find that the NoMelt seismic models require a large increase in the frequency of the EAGBS peak between 60 km and 80 km (Fig. 8e). At depths <= 60 km, the low attenuation and high velocity require that the EAGBS peak has almost no effect, which means that it exists at very low frequencies or not at all. At depths >= 80 km, the low velocities require that the shear modulus is relaxed in the seismic band, and the moderate attenuation exerts strong control over the possible frequency range for the EAGBS peak. Both the velocity and attenuation models undergo large changes around depth =70 km that cannot be more precisely located in depth; thus we restrict our interpretation to depths <= 60 km and >= 80

km. We have also determined the allowable peak frequencies for the smooth velocity models and for the two different treatments of radial anisotropy (i.e., all four V_S models in Fig. 6c); in all cases a large change in peak frequency is required at 60-80 km.

What factors could cause the frequency of the peak (f_e) to shift by several orders of magnitude over < 20 km in depth? We assume that the attenuation peak is due to EAGBS and recall that $f_e = 1/\tau_e = \mu_U \delta / \eta_{gb} d$. There is no reason to expect such large changes in grain size or unrelaxed shear modulus over this depth interval. Instead, the properties of the grain boundary must change. If η_{gb} decreases by a factor of 10^3 then f_e increases by a factor of 10^3. A likely explanation is an increase in the water content of the upper mantle in addition to the increase in temperature, which has been proposed to reduce grain-boundary viscosity (Karato, 2012). A change in water content is also consistent with electrical conductivity measurements from the study region, which suggest ∼150 ppm H_2O at 150-km depth and negligible H_2O at depths <90 km (Sarafian et al., 2015).

An additional consideration is partial melt. Jackson et al. (2004) and Faul et al. (2004) showed that small degrees of melt would enhance the level of HTB and introduce a high-frequency peak, thus changing the shape of the frequency dependence. Given that NoMelt asthenospheric attenuation is moderate and weaker than the asthenospheric attenuation measured at the East Pacific Rise (Yang et al., 2007) and Juan de Fuca ridge (Ruan et al., 2018), we conclude that our results are not consistent with an important role for melt. Similarly, Sarafian et al. (2015) concluded that their NoMelt electrical structure does not support the presence of melt at asthenospheric depths; furthermore, the expected temperature profile does not cross the anhydrous solidus. However, we cannot rule out a small amount of melt that is distributed such that it minimally affects attenuation in the seismic band and electrical conductivity.

6. Conclusions

A two-plane wave method is used to constrain the average Rayleigh wave amplitude decay across the NoMelt array in the period range 33-100 sec. Removal of tilt and compliance noise allows a large number of events (∼125) to be measured. The measurements are well fit by a two −layer model: a shallow layer with $Q_\mu = 1400$, a deeper layer with $Q_\mu = 110$, and a transition depth at 70 km. An inversion for fully depth-dependent attenuation, conducted using this two-layer model as a starting model, shows only minor deviations from this simple structure. Although Rayleigh waves cannot resolve sharp depth gradients, the transition from low attenuation at shallow depths to moderate attenuation at greater depths occurs over a fairly narrow depth range, ∼60-80 km. When these newly obtained values of Q_μ are compared with the intrinsic attenuation values measured at higher frequency (∼3 Hz, Takeuchi et al., 2017), the difference in the frequency dependences of Q_μ between lithosphere and asthenosphere is much smaller than what was suggested by Takeuchi et al. (2017). This revises their interpretation that the frequency dependence of attenuation differs between the lithosphere and asthenosphere.

We also develop a new shear-velocity model for the NoMelt area using the Rayleigh and Love wave phase velocities from Lin et al. (2016) and Russell et al. (2019). A 5% velocity reduction over the depth range 60-65 km is imposed in order to satisfy constraints from an Sp receiver function study (Mark et al., 2019). We estimate the effect of anelasticity on shear velocity through comparison to predictions of anharmonic velocity obtained using realistic thermal and compositional structures. This comparison reveals that the depth of the velocity minimum observed with NoMelt data is greater than the depth at which the conductive thermal boundary layer joins with the mantle adiabat, suggesting

that anelastic effects may shift this feature in depth and possibly complicate efforts to infer thermal structure from the shape of the low-velocity zone.

We use laboratory-based parameters to predict attenuation and velocity-dispersion spectra that result from the superposition of a weakly frequency dependent high-temperature background and an absorption peak. We adopt the form described in Jackson and Faul (2010) but test a large range of frequencies for the position of the absorption peak (f_e). We then determine, at each depth, which values of f_e predict Q_μ and V_S that can fit the NoMelt Q_μ and V_S values simultaneously. We show that between depths of 60 and 80 km the seismic models require an increase in f_e by at least 3-4 orders of magnitude. Under the assumption that the absorption peak is caused by elastically accommodated grain-boundary sliding, this increase in f_e reflects a decrease in grain-boundary viscosity of 3-4 orders of magnitude. A likely explanation is an increase in the water content of the mantle, with the base of the dehydrated lid located at ∼70-km depth.

Declaration of competing interest

The authors declare that they have no known competing financial interests or personal relationships that could have appeared to influence the work reported in this paper.

Acknowledgement

Appendix A. Supplementary material

Supplementary material related to this article can be found online at https://doi.org/10.1016/j.epsl.2020.116148.

References

Abers, G.A., Fischer, K.M., Hirth, G., Wiens, D.A., Plank, T., Holtzman, B.K., McCarthy, C., Gazel, E., 2014. Reconciling mantle attenuation-temperature relationships from seismology, petrology, and laboratory measurements. Geochem. Geophys. Geosyst. 15 (9), 3521–3542.

Aizawa, Y., Barnhoorn, A., Faul, U.H., Fitz Gerald, J.D., Jackson, I., Kovács, I., 2008. Seismic properties of Anita Bay dunite: an exploratory study of the influence of water. J. Petrol. 49 (4), 841–855.

Bell, S.W., Forsyth, D.W., Ruan, Y., 2014. Removing noise from the vertical component records of ocean-bottom seismometers: results from year one of the Cascadia Initiative. Bull. Seismol. Soc. Am. 105 (1), 300–313.

Cline II, C.J., Faul, U.H., David, E.C., Berry, A.J., Jackson, I., 2018. Redox-influenced seismic properties of upper-mantle olivine. Nature 555 (7696), 355.

Connolly, J.A.D., 2009. The geodynamic equation of state: what and how. Geochem. Geophys. Geosyst. 10 (10).

Cooper, R.F., 2002. Seismic wave attenuation: energy dissipation in viscoelastic crystalline solids. Rev. Mineral. Geochem. 51 (1), 253–290.

Dalton, C.A., Bao, X., Ma, Z., 2017. The thermal structure of cratonic lithosphere from global Rayleigh wave attenuation. Earth Planet. Sci. Lett. 457, 250–262.

Dalton, C.A., Ekström, G., Dziewoński, A.M., 2008. The global attenuation structure of the upper mantle. J. Geophys. Res., Solid Earth 113 (B9).

Dalton, C.A., Langmuir, C.H., Gale, A., 2014. Geophysical and geochemical evidence for deep temperature variations beneath mid-ocean ridges. Science 344 (6179), 80–83.

Desonie, D.L., Duncan, R.A., 1990. The Cobb-Eickelberg seamount chain: hotspot volcanism with mid-ocean ridge basalt affinity. J. Geophys. Res., Solid Earth 95 (B8), 12697–12711.

Durek, J.J., Ekström, G., 1996. A radial model of anelasticity consistent with long-period surface-wave attenuation. Bull. Seismol. Soc. Am. 86 (1A), 144–158.

Dziewonski, A.M., Anderson, D.L., 1981. Preliminary reference Earth model. Phys. Earth Planet. Inter. 25 (4), 297–356.

Ekström, G., Nettles, M., Dziewoński, A.M., 2012. The global CMT project 2004–2010: centroid-moment tensors for 13,017 earthquakes. Phys. Earth Planet. Inter. 200, 1–9.

Faul, U., Jackson, I., 2015. Transient creep and strain energy dissipation: an experimental perspective. Annu. Rev. Earth Planet. Sci. 43, 541–569.

Faul, U.H., Fitz Gerald, J.D., Jackson, I., 2004. Shear wave attenuation and dispersion in melt-bearing olivine polycrystals: 2. Microstructural interpretation and seismological implications. J. Geophys. Res., Solid Earth 109 (B6).

Forsyth, D.W., 1992. Geophysical constraints on mantle flow and melt generation beneath mid-ocean ridges. In: Mantle Flow and Melt Generation at Mid-Ocean Ridges, vol. 71, pp. 1–65.

Forsyth, D.W., Li, A., 2005. Array analysis of two-dimensional variations in surface wave phase velocity and azimuthal anisotropy in the presence of multipathing interference. In: Seismic Earth: Array Analysis of Broadband Seismograms, vol. 157, pp. 81–97.

Foster, A., Nettles, M., Ekström, G., 2014. Overtone interference in array-based Lovewave phase measurements. Bull. Seismol. Soc. Am. 104 (5), 2266–2277.

Freed, A.M., Hirth, G., Behn, M.D., 2012. Using short-term postseismic displacements to infer the ambient deformation conditions of the upper mantle. J. Geophys. Res., Solid Earth 117 (B1).

French, S., Lekic, V., Romanowicz, B., 2013. Waveform tomography reveals channeled flow at the base of the oceanic asthenosphere. Science 342 (6155), 227–230.

Gaherty, J.B., Jordan, T.H., Gee, L.S., 1996. Seismic structure of the upper mantle in a central Pacific corridor. J. Geophys. Res., Solid Earth 101 (B10), 22291–22309.

Garapic, G., Faul, U.H., Brisson, E., 2013. High-resolution imaging of the melt distribution in partially molten upper mantle rocks: evidence for wetted two-grain boundaries. Geochem. Geophys. Geosyst. 14 (3), 556–566.

Gribb, T.T., Cooper, R.F., 1998. Low-frequency shear attenuation in polycrystalline olivine: grain boundary diffusion and the physical significance of the Andrade model for viscoelastic rheology. J. Geophys. Res., Solid Earth 103 (B11), 27267–27279.

Harmon, N., Rychert, C.A., 2016. Joint inversion of teleseismic and ambient noise Rayleigh waves for phase velocity maps, an application to Iceland. J. Geophys. Res., Solid Earth 121 (8), 5966–5987.

Hirth, G., Kohlstedt, D.L., 1996. Water in the oceanic upper mantle: implications for rheology, melt extraction and the evolution of the lithosphere. Earth Planet. Sci. Lett. 144 (1–2), 93–108.

Jackson, I., Faul, U.H., 2010. Grainsize-sensitive viscoelastic relaxation in olivine: towards a robust laboratory-based model for seismological application. Phys. Earth Planet. Inter. 183 (1–2), 151–163.

Jackson, I., Faul, U.H., Fitz Gerald, J.D., Tan, B.H., 2004. Shear wave attenuation and dispersion in melt-bearing olivine polycrystals: 1. Specimen fabrication and mechanical testing. J. Geophys. Res., Solid Earth 109 (B6).

Jackson, I., Faul, U.H., Skelton, R., 2014. Elastically accommodated grain-boundary sliding: new insights from experiment and modeling. Phys. Earth Planet. Inter. 228, 203–210.

Karato, S.I., 2012. On the origin of the asthenosphere. Earth Planet. Sci. Lett. 321, 95–103.

Karato, S.I., Park, J., 2019. On the origin of the upper mantle seismic discontinuities. In: Lithospheric Discontinuities, vol. 239, p. 5.

Kawakatsu, H., Kumar, P., Takei, Y., Shinohara, M., Kanazawa, T., Araki, E., Suyehiro, K., 2009. Seismic evidence for sharp lithosphere-asthenosphere boundaries of oceanic plates. Science 324 (5926), 499–502.

Lee, C.T.A., Lenardic, A., Cooper, C.M., Niu, F., Levander, A., 2005. The role of chemical boundary layers in regulating the thickness of continental and oceanic thermal boundary layers. Earth Planet. Sci. Lett. 230 (3–4), 379–395.

Lin, P.Y.P., Gaherty, J.B., Jin, G., Collins, J.A., Lizarralde, D., Evans, R.L., Hirth, G., 2016. High-resolution seismic constraints on flow dynamics in the oceanic asthenosphere. Nature 535 (7613), 538.

Liu, H.P., Anderson, D.L., Kanamori, H., 1976. Velocity dispersion due to anelasticity; implications for seismology and mantle composition. Geophys. J. Int. 47 (1), 41–58.

Ma, Z., Dalton, C.A., 2019. Evidence for dehydration-modulated small-scale convection in the oceanic upper mantle from seafloor bathymetry and Rayleigh wave phase velocity. Earth Planet. Sci. Lett. 510, 12–25.

Mark, H.F., Lizarralde, D., Collins, J.A., Miller, N.C., Hirth, G., Gaherty, J.B., Evans, R.L., 2019. Azimuthal seismic anisotropy of 70-Ma Pacific-plate upper mantle. J. Geophys. Res., Solid Earth.

Mei, S., Kohlstedt, D.L., 2000. Influence of water on plastic deformation of olivine aggregates: 1. Diffusion creep regime. J. Geophys. Res., Solid Earth 105 (B9), 21457–21469.

Nishimura, C.E., Forsyth, D.W., 1989. The anisotropic structure of the upper mantle in the Pacific. Geophys. J. Int. 96 (2), 203–229.

Olugboji, T.M., Karato, S.I., Park, J., 2013. Structures of the oceanic lithosphere-asthenosphere boundary: mineral-physics modeling and seismological signatures. Geochem. Geophys. Geosyst. 14 (4), 880–901.

Parsons, B., Sclater, J.G., 1977. An analysis of the variation of ocean floor bathymetry and heat flow with age. J. Geophys. Res. 82 (5), 803–827.

Ruan, Y., Forsyth, D.W., Bell, S.W., 2018. Shear attenuation beneath the Juan de Fuca plate: implications for mantle flow and dehydration. Earth Planet. Sci. Lett. 496, 189–197.

Russell, J.B., Gaherty, J.B., Lin, P.Y.P., Lizarralde, D., Collins, J.A., Hirth, G., Evans, R.L., 2019. High-resolution constraints on Pacific upper mantle petrofabric inferred from surface-wave anisotropy. J. Geophys. Res., Solid Earth 124 (1), 631–657.

Rychert, C.A., Shearer, P.M., 2011. Imaging the lithosphere-asthenosphere boundary beneath the Pacific using SS waveform modeling. J. Geophys. Res., Solid Earth 116 (B7).

Sarafian, E., Evans, R.L., Collins, J.A., Elsenbeck, J., Gaetani, G.A., Gaherty, J.B., Hirth, G., Lizarralde, D., 2015. The electrical structure of the central Pacific upper mantle constrained by the NoMelt experiment. Geochem. Geophys. Geosyst. 16 (4), 1115–1132.

Sasaki, Y., Takei, Y., McCarthy, C., Rudge, J.F., 2019. Experimental study of dislocation damping using a rock analogue. J. Geophys. Res., Solid Earth 124 (7), 6523–6541.

Schmerr, N., 2012. The Gutenberg discontinuity: melt at the lithosphere-asthenosphere boundary. Science 335 (6075), 1480–1483.

Stein, C.A., Stein, S., 1992. A model for the global variation in oceanic depth and heat flow with lithospheric age. Nature 359 (6391), 123.

Stixrude, L., Lithgow-Bertelloni, C., 2011. Thermodynamics of mantle minerals-II. Phase equilibria. Geophys. J. Int. 184 (3), 1180–1213.

Sundberg, M., Cooper, R.F., 2010. A composite viscoelastic model for incorporating grain boundary sliding and transient diffusion creep; correlating creep and attenuation responses for materials with a fine grain size. Philos. Mag. 90 (20), 2817–2840.

Takeuchi, N., Kawakatsu, H., Shiobara, H., Isse, T., Sugioka, H., Ito, A., Utada, H., 2017. Determination of intrinsic attenuation in the oceanic lithosphere-asthenosphere system. Science 358 (6370), 1593–1596.

Warren, J.M., 2016. Global variations in abyssal peridotite compositions. Lithos 248, 193–219.

Wei, S.S., Wiens, D.A., 2018. P-wave attenuation structure of the Lau back-arc basin and implications for mantle wedge processes. Earth Planet. Sci. Lett. 502, 187–199.

Workman, R.K., Hart, S.R., 2005. Major and trace element composition of the depleted MORB mantle (DMM). Earth Planet. Sci. Lett. 231 (1–2), 53–72.

Yamauchi, H., Takei, Y., 2016. Polycrystal anelasticity at near-solidus temperatures. J. Geophys. Res., Solid Earth 121 (11), 7790–7820.

Yang, Y., Forsyth, D.W., 2006. Regional tomographic inversion of the amplitude and phase of Rayleigh waves with 2-D sensitivity kernels. Geophys. J. Int. 166 (3), 1148–1160.

Yang, Y., Forsyth, D.W., Weeraratne, D.S., 2007. Seismic attenuation near the East Pacific Rise and the origin of the low-velocity zone. Earth Planet. Sci. Lett. 258 (1–2), 260–268.